coatings

MDPI

*Article*

# Effects of Bias Voltage and Substrate Temperature on the Mechanical Properties and Oxidation Behavior of CrWSiN Films

**Li-Chun Chang [1,2], Chin-Han Tzeng [3], Tzu-Yu Ou [3] and Yung-I Chen [3,4,*]**

[1] Department of Materials Engineering, Ming Chi University of Technology, New Taipei 243303, Taiwan; lcchang@mail.mcut.edu.tw
[2] Center for Plasma and Thin Film Technologies, Ming Chi University of Technology, New Taipei 243303, Taiwan
[3] Department of Optoelectronics and Materials Technology, National Taiwan Ocean University, Keelung 202301, Taiwan; 11089003@email.ntou.edu.tw (C.-H.T.); outzuyu23@gmail.com (T.-Y.O.)
[4] Center of Excellence for Ocean Engineering, National Taiwan Ocean University, Keelung 202301, Taiwan
* Correspondence: yichen@mail.ntou.edu.tw

**Abstract:** CrWSiN films were prepared through the co-sputtering technique, and the process variables were substrate bias voltage and temperature. The mechanical properties of hardness and elastic modulus of the CrWSiN films were dominantly affected by their average crystallite size and by substrate bias voltage and temperature. Moreover, the effect of substrate temperature was more evident than that of substrate bias. The highest hardness and elastic modulus of 42.6 and 459 GPa, respectively, were obtained for the $Cr_{20}W_{28}Si_9N_{43}$ film fabricated at a substrate temperature of 400 °C, which exhibits an evident advantage over the 25.0 and 323 GPa values for the $Cr_{21}W_{28}Si_9N_{42}$ film fabricated at room temperature. In contrast, an increase in negative bias voltage to −100 V on the substrate decreased the mechanical properties compared to one prepared using a similar process without applying the negative bias voltage. The oxidation resistance of the Cr-enriched $Cr_{37}W_4Si_{10}N_{49}$ and $Cr_{37}W_5Si_{10}N_{48}$ films was superior to that of the $Cr_{20}W_{28}Si_9N_{43}$ films with near-equal Cr and W contents annealed at 900 °C in air. The formation of a surficial $Cr_2O_3$ layer plays a vital role in restricting subsequent oxidation for CrWSiN films.

**Keywords:** co-sputtering; mechanical properties; oxidation; wear resistance

check for updates

**Citation:** Chang, L.-C.; Tzeng, C.-H.; Ou, T.-Y.; Chen, Y.-I. Effects of Bias Voltage and Substrate Temperature on the Mechanical Properties and Oxidation Behavior of CrWSiN Films. *Coatings* **2023**, *13*, 1672. https://doi.org/10.3390/coatings13101672

Academic Editors: Manuel António Peralta Evaristo and Panos Poulopoulos

Received: 31 July 2023
Revised: 19 September 2023
Accepted: 22 September 2023
Published: 24 September 2023

**Copyright:** © 2023 by the authors. Licensee MDPI, Basel, Switzerland. This article is an open access article distributed under the terms and conditions of the Creative Commons Attribution (CC BY) license (https://creativecommons.org/licenses/by/4.0/).

## 1. Introduction

The mechanical and antioxidative properties of transition metal nitride thin films are enhanced by the addition of Si, according to the literature on CrSiN [1,2], WSiN [3,4], and CrAlSiN [5,6] films. Si atoms doped into transition metal nitride lattices play the roles of substitutional or interstitial atoms, resulting in the solid solution strengthening of mechanical properties [1,3]. Moreover, the formation of amorphous $SiN_x$ establishes nanocomposite structures, reduces crystallite sizes, and hinders the movement of dislocations, which enhances the mechanical properties related to specific Si contents [7]. In the work of Lee and Chang [8], the CrSiN film with 10.1 at.% Si formed a nanocomposite structure and had a hardness of 24.6 GPa. Moreover, Ju et al. [3] reported that nanocomposite WSiN films with a Si content of 23.5 at.% presented a high hardness value of 40 GPa. In a previous study [9], CrWSiN thin films were explored to combine the mechanical properties of WSiN films and the antioxidative properties of CrSiN films. The formation enthalpy at 298 K is −22 kJ/mol [10] for $W_2N$, which is not as large as the values of −744.8 and −117.2 kJ/mol for $Si_3N_4$ and CrN [11], respectively. These CrWSiN films are under-stoichiometric due to the low affinity between W and N. The structures of CrWSiN thin films are categorized into crystalline CrSiN-, amorphous WSiN-, and amorphous $SiN_x$-dominated structures

depending on their chemical compositions, and the films mentioned above exhibited distinct mechanical and antioxidative properties. The $Cr_{21}W_{28}Si_9N_{42}$ films with comparable Cr and W contents exhibit a CrSiN-dominated structure, accompanied by a hardness of 25 GPa and an elastic modulus of 323 GPa, which are the highest mechanical properties among those of the investigated CrWSiN films [9]. In contrast, the CrSiN-dominated $Cr_{39}W_5Si_9N_{47}$ films with Cr-enriched content exhibit a hardness of 8.6 GPa and an elastic modulus of 208 GPa, demonstrating the lowest mechanical properties [9]. Moreover, an improved oxidation resistance at 800 °C was achieved for the $Cr_{21}W_{28}Si_9N_{42}$ films due to the formation of surficial $Cr_2WO_6$ scale [9,12]. Mechanical and tribological properties are crucial for films utilized as hard coatings [13,14], whereas antioxidative properties are vital for films applied at high temperatures [5,6]. Applying substrate bias voltage ($V_B$) and elevated substrate temperature ($T_S$) are essential process parameters in sputtering technology that improve the characteristics of nitride thin films [15,16]. In a previous study [16], the phase, texture, and bonding characteristics of CrSiN films with a Si level of 14 at.% were not influenced by $V_B$ and $T_S$, whereas the lattice constants and crystallite sizes were affected by $V_B$ and $T_S$. The CrSiN films fabricated at a $V_B$ of −100 V and a $T_S$ of 400 °C demonstrated a hardness of 22.2 GPa and an elastic modulus of 299 GPa, which are superior to the values of 13.4 and 223 GPa for films fabricated at the grounded state and room temperature. The competition between grain growth and nucleation rates of the CrSiN films affects their crystallite sizes and mechanical properties [16,17]. Generally, raising the substrate temperature causes higher adatom mobility, resulting in a higher growth rate and crystallite size [18,19]. However, at much higher temperatures, high kinetic energy enhances atomic diffusion and collision, resulting in higher nucleation rates and reduced crystallite size [18,20]. Therefore, exploring the influences of $V_B$ and $T_S$ on the mechanical and antioxidative properties of CrWSiN films is vital. The aforementioned $Cr_{21}W_{28}Si_9N_{42}$ and $Cr_{39}W_5Si_9N_{47}$ films can be recognized as W and Si co-incorporated CrN films, but they exhibit distinct mechanical properties. Modifying the sputtering processes for fabricating $Cr_{21}W_{28}Si_9N_{42}$ and $Cr_{39}W_5Si_9N_{47}$ films by applying $V_B$ and $T_S$ has become a key research topic. In this study, CrWSiN films were fabricated through sputtering with $V_B$ values of 0 to −150 V and $T_S$ values of room temperature to 400 °C. The fabricated films' mechanical properties and wear resistance were examined, and their oxidation behavior was inspected in ambient air at 800 and 900 °C.

## 2. Materials and Methods

The preparation of CrWSiN films with a Cr interlayer through co-sputtering was described in a previous study [9]. Direct current powers were applied to Cr, W, and Si targets. The targets mentioned above were 50.8 mm in diameter. Two batches (Batch 50 and Batch 90) of CrWSiN films were fabricated. The Batch 50 films, including samples A50, A50B(50), A50B(100), A50B(150), A50T(300), A50T(400), and A50BT, were prepared by applying DC powers of 50 W on each target ($P_{Cr}$ = $P_W$ = $P_{Si}$ = 50 W). In contrast, the Batch 90 films, including A90, A90B(100), A90T(400), and A90BT, were fabricated with $P_{Cr}$ = 90 W, $P_W$ = 10 W, and $P_{Si}$ = 50 W. Samples A50 and A90 were prepared using electrically grounded substrates without additional heating. Samples A50B(100) and A90B(100) were manufactured with a substrate bias ($V_B$) of −100 V and without heating. Samples A50T(400) and A90T(400) were fabricated in a grounded state and a substrate temperature ($T_S$) of 400 °C, whereas samples A50BT and A90BT were produced at $V_B$ = −100 V and $T_S$ = 400 °C. Three more Batch 50 samples, A50B(50), A50B(150), and A50T(300), prepared at a $V_B$ of −50 V, $V_B$ of −150 V, and a $T_S$ of 300 °C, respectively, were included in the discussion of chemical compositions, deposition rates, and mechanical properties. The antioxidative properties of CrWSiN films were evaluated after annealing in air at 800 and 900 °C for 2 h.

The chemical compositions of the CrWSiN films were determined using a field-emission electron probe microanalyzer (JXA-iHP200F, JEOL, Tokyo, Japan). The phases and texture in the films were identified using grazing incident and Bragg–Brentano (θ–2θ)

X-ray diffraction (X'Pert PRO MPD, PANalytical, Almelo, the Netherlands), respectively. The texture coefficients $T_c(111)$ and $T_c(200)$ were calculated using the Bragg–Brentano X-ray diffraction (BBXRD) patterns as follows:

$$T_c(hkl) = \frac{I_m(hkl)}{I_0(hkl)} \left[ \frac{1}{n} \sum_{n=1}^{n} \frac{I_m(hkl)}{I_0(hkl)} \right]^{-1}, \quad (1)$$

where $I_m$ and $I_0$ are the measured and standard relative intensities of the (*hkl*) reflection [21], respectively, and $n = 2$ as (111) and (200) reflections were considered. The average crystallite sizes of the CrWSiN films were calculated following Scherrer's formula [22] using the (111) reflections in the BBXRD patterns. The samples with a protective Pt layer for transmission electron microscopy (TEM) observation were prepared using a focused ion beam system (NX2000, Hitachi, Tokyo, Japan). The mechanical properties, hardness and reduced elastic modulus ($E_r$), of the films were measured using a nanoindentation tester (TI-900 Triboindenter, Hysitron, Eden Prairie, MN, USA) and determined using the Oliver–Pharr method [23]. The elastic modulus ($E$) of a film was derived from

$$\frac{1}{E_r} = \frac{1 - \nu^2}{E} + \frac{1 - \nu_i^2}{E_i}, \quad (2)$$

where $E_i$ (1141 GPa) is the elastic modulus and $\nu_i$ (0.07) is Poisson's ratio of the indenter [24]. The Poisson ratio of the CrWSiN films ($v$) was assumed to be 0.25 [9]. The Poisson ratios of CrN, $W_2N$, and $Si_3N_4$ were 0.24 [25], 0.29 [26], and 0.26 [27], respectively. The residual stress in the films was estimated using the curvature method [28]. The wear resistance of the films was evaluated through the pin-on-disk test [9].

## 3. Results and Discussion

### *3.1. Chemical Compositions and Phase Structures*

Table 1 lists the chemical compositions of the CrWSiN films. The O contents were 0–0.8 and 1.7–3.4 at.% in the Batch 50 and 90 samples, respectively, which implies that the O pollution was contributed by the high chemical affinity between Cr and residual O in the sputter chamber since the Batch 90 samples were Cr-enriched. The O content was ignored in this study. The Batch 50 samples exhibited a chemical composition of 20–26 at.% Cr—20–28 at.% W—7–10 at.% Si—42–47 at.% N, denoted as $Cr_{20–26}W_{20–28}Si_{7–10}N_{42–47}$, whereas the Batch 90 samples showed $Cr_{37–41}W_{4–5}Si_{8–10}N_{47–49}$. The process parameters, $V_B$ and $T_S$, exhibited limited effects on these samples' constitutions. The process with a negative bias on the substrate first increased and then decreased the deposition rate by increasing the bias voltage related to that prepared with a grounded substrate. For example, the deposition rate of the A50B(50) sample was 6.4 nm/min, which is higher than the 5.9 nm/min of the A50 sample. Moreover, the deposition rate decreased from 6.4 to 6.1 and 5.2 nm/min with an increase in the bias voltage from −50 to −100 and −150 V due to resputtering [16,29]. The A50T(300) films exhibited a deposition rate of 6.0 nm/min, similar to that of the A50 films, whereas the A50T(400) sample showed a lower deposition rate of 5.4 nm/min. The higher substrate temperature enhances the adatom mobility and raises the evaporation rate, which decreases the deposition rate [20].

Figure 1a,b displays the grazing incident X-ray diffraction (GIXRD) patterns of the Batch 50 and 90 samples, respectively. All the CrWSiN films exhibited a face-centered cubic (fcc) solid solution consisting of CrN and $W_2N$ components with evident (111), (200), (220), and (311) reflections. Moreover, (222) reflections were observed for the A50T(400) and A50BT samples. The lattice constants were 0.4188 and 0.4146 nm for the A50 and A90 samples. The lattice constants decreased to lower levels after applying the substrate bias or substrate temperature, except for in the A50B(150) sample (Table 2). The lattice constants decreased from 0.4188 nm for the A50 sample to 0.4186, 0.4184, 0.4182, 0.4186, and 0.4182 nm for the A50B(50), A50B(100), A50T(300), A50T(400), and A50BT samples, respectively, whereas the lattice constants decreased from 0.4146 nm for the A90 sample to 0.4143, 0.4139, and 0.4139 nm

for the A90B(100), A90T(400), and A90BT samples, respectively. The reflection shifts in XRD patterns were related to the variation in lattice constants of the films. These changes were not evident in the samples within batches due to small deviations in their chemical compositions. However, the lattice constants of the Batch 90 samples (0.4139–0.4146 nm) were lower than those of the Batch 50 samples (0.4182–0.4193 nm), which was attributed to a lower W content for the Batch 90 samples. Moreover, Benkahoul et al. [7] reported that CrSiN films with a Cr content of 6.7–11.6 at.% exhibited a nanocomposite structure in which amorphous $SiN_x$ phase surrounded the crystallites. Figure 2a,b displays the BBXRD patterns of the Batch 50 and 90 samples, respectively. All the CrWSiN films exhibited an fcc phase, and the Cr (110) reflections contributed from the interlayers were observed. The Cr (200) reflection was observed at a two-theta angle of 64°, not shown in Figure 2. The texture coefficients indicate that all the films exhibited a (111) orientation (Table 2). Table 2 shows the average crystallite sizes of CrWSiN films determined using the full width at half maximum (FWHM) of the (111) reflections. The crystallite size of the A50 sample was 44 nm, whereas the A50B(50) and A50B(100) exhibited a larger size of 51 nm, and the A50B(150) sample exhibited a crystallite size of 43 nm. The A50T(300) and A50T(400) showed crystallite sizes of 47 and 37 nm, respectively, which reveals distinct effects contributed by grain growth and nucleation [16]. The CrSiN films prepared at room temperature, 300, and 400 °C exhibited average crystallite sizes of 16.2, 19.2, and 14.1 nm [16], respectively. The crystallite sizes of the Batch 90 samples revealed a similar variation trend. The A90 sample exhibited an average crystallite size of 62 nm, whereas the A90B(100) prepared through a biased process exhibited a higher value of 77 nm, and the A90T(400) produced at an elevated temperature of 400 °C revealed a lower value of 37 nm. The crystallite size affected the mechanical properties of the films, which is further discussed in Section 3.2.

**Table 1.** Chemical compositions, deposition rate, and thicknesses of the CrWSiN films.

| Sample | | Chemical Composition (at.%) | | | | | $R$ [1] | $T$ [2] |
|---|---|---|---|---|---|---|---|---|
| | | Cr | W | Si | N | O | (nm/min) | (nm) |
| A50 | $Cr_{21}W_{28}Si_9N_{42}$ | 20.9 ± 0.3 | 27.6 ± 0.2 | 9.4 ± 0.1 | 41.5 ± 0.4 | 0.6 ± 0.2 | 5.9 | 705 |
| A50B(50) | $Cr_{26}W_{20}Si_7N_{47}$ | 25.5 ± 0.4 | 20.3 ± 0.4 | 6.8 ± 0.3 | 46.6 ± 1.2 | 0.8 ± 0.2 | 6.4 | 831 |
| A50B(100) | $Cr_{24}W_{25}Si_9N_{42}$ | 24.3 ± 0.0 | 25.0 ± 0.2 | 8.5 ± 0.1 | 42.0 ± 0.1 | 0.2 ± 0.2 | 6.1 | 794 |
| A50B(150) | $Cr_{22}W_{24}Si_8N_{46}$ | 22.0 ± 0.5 | 24.0 ± 0.2 | 7.6 ± 0.2 | 46.1 ± 0.8 | 0.3 ± 0.2 | 5.2 | 679 |
| A50T(300) | $Cr_{23}W_{25}Si_7N_{45}$ | 22.5 ± 0.1 | 25.3 ± 0.2 | 6.5 ± 0.4 | 45.2 ± 0.7 | 0.5 ± 0.2 | 6.0 | 778 |
| A50T(400) | $Cr_{20}W_{28}Si_9N_{43}$ | 20.2 ± 0.3 | 27.6 ± 0.4 | 9.4 ± 0.1 | 42.8 ± 0.7 | 0.0 ± 0.0 | 5.4 | 700 |
| A50BT | $Cr_{21}W_{28}Si_{10}N_{42}$ | 20.9 ± 0.4 | 28.1 ± 0.4 | 9.5 ± 0.4 | 41.5 ± 1.0 | 0.0 ± 0.0 | 5.5 | 719 |
| A90 | $Cr_{39}W_5Si_9N_{47}$ | 38.2 ± 0.4 | 4.2 ± 0.1 | 8.9 ± 0.0 | 47.0 ± 0.3 | 1.7 ± 0.1 | 6.8 | 880 |
| A90B(100) | $Cr_{41}W_4Si_8N_{47}$ | 40.3 ± 0.3 | 3.9 ± 0.2 | 7.9 ± 0.0 | 46.0 ± 0.5 | 1.9 ± 0.2 | 7.2 | 937 |
| A90T(400) | $Cr_{37}W_4Si_{10}N_{49}$ | 35.4 ± 0.2 | 4.3 ± 0.0 | 9.3 ± 0.1 | 47.6 ± 0.4 | 3.4 ± 0.2 | 5.4 | 701 |
| A90BT | $Cr_{37}W_5Si_{10}N_{48}$ | 35.9 ± 0.3 | 4.4 ± 0.2 | 9.7 ± 0.1 | 47.0 ± 0.4 | 3.0 ± 0.2 | 7.2 | 937 |

[1] $R$: deposition rate. [2] $T$: thickness.

**Table 2.** Lattice constants, texture coefficients, and average crystallite sizes of the CrWSiN films.

| Sample | Lattice Constants | $T_c$(111) [1] | $T_c$(200) [1] | Crystallite Size |
|---|---|---|---|---|
| | (nm) | | | (nm) |
| A50 | 0.4188 | 1.96 | 0.04 | 44 |
| A50B(50) | 0.4186 | 1.99 | 0.01 | 51 |
| A50B(100) | 0.4184 | 1.99 | 0.01 | 51 |
| A50B(150) | 0.4193 | 1.95 | 0.05 | 43 |
| A50T(300) | 0.4182 | 1.80 | 0.20 | 47 |
| A50T(400) | 0.4186 | 1.71 | 0.29 | 37 |
| A50BT | 0.4182 | 1.44 | 0.56 | 25 |
| A90 | 0.4146 | 1.94 | 0.06 | 62 |
| A90B(100) | 0.4143 | 2.00 | 0.00 | 77 |
| A90T(400) | 0.4139 | 1.87 | 0.13 | 37 |
| A90BT | 0.4139 | 1.91 | 0.09 | 40 |

[1] $T_c$(111), $T_c$(200): texture coefficients of reflections (111) and (200).

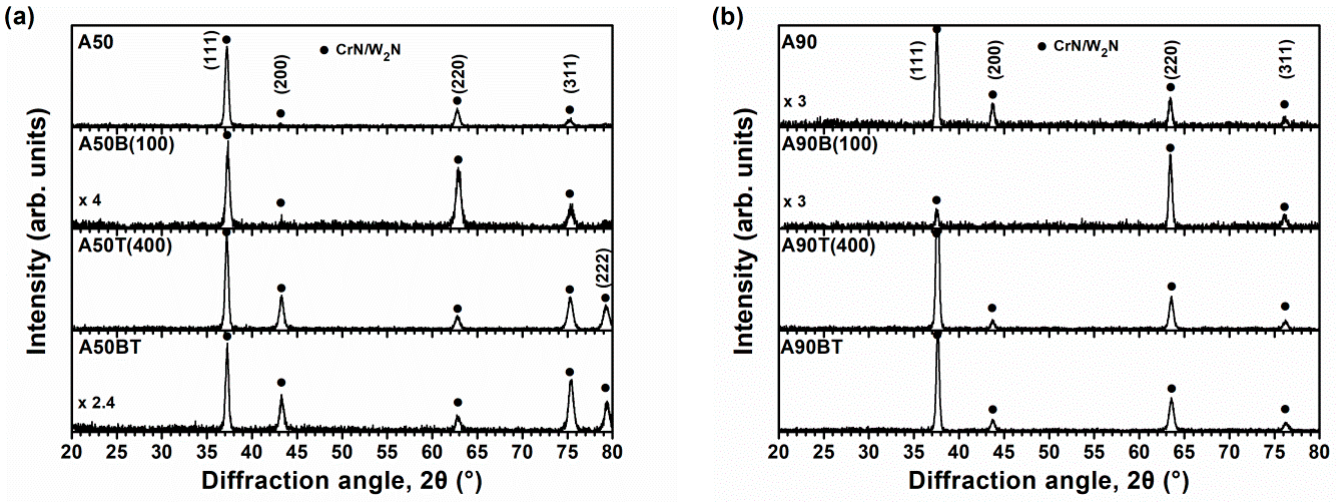


**Figure 1.** GIXRD patterns of (**a**) Batch 50 and (**b**) Batch 90 samples.

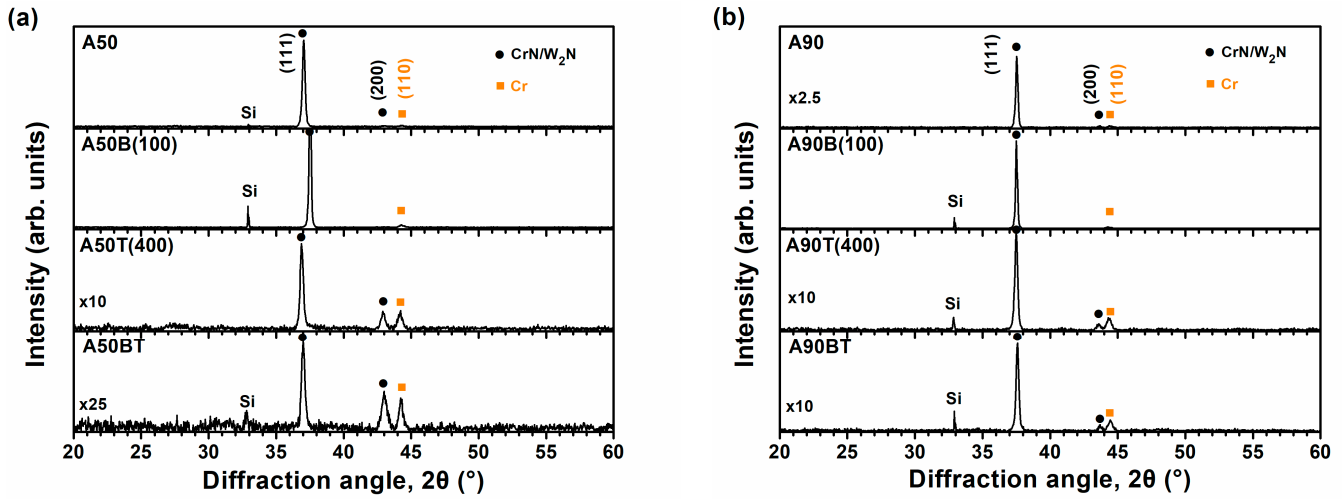


**Figure 2.** BBXRD patterns of (**a**) Batch 50 and (**b**) Batch 90 samples.

Figure 3a exhibits a cross-sectional TEM (XTEM) image of the A50T(400) sample, which reveals a tight columnar structure. The selected area electron diffraction (SAED) pattern of the A50T(400) sample (Figure 3b) shows an fcc phase with diffraction spots (111), (200), and (220), which represent *d*-spacing values of 0.242, 0.211, and 0.150 nm, respectively. Figure 3c exhibits a high-resolution TEM (HRTEM) image of the A50T(400) sample, which displays lattice fringes corresponding to *d*-spacing values of 0.210–0.215 nm for the fcc (200) planes. Figure 4a depicts an XTEM image of the A90B(100) sample, revealing a columnar structure with stripes between the grains. The SAED pattern of the A90B(100) sample (Figure 4b) reveals an fcc phase similar to that of the A50T(400) sample (Figure 3b). Moreover, the stripes at the interfaces between crystalline grains were identified to be amorphous in the HRTEM image (Figure 4c). These amorphous stripes could affect the residual stress and mechanical properties of the films. The amorphous $SiN_x$ phase with low density and disordered structure decreased the compressive residual stress and hardness [3].

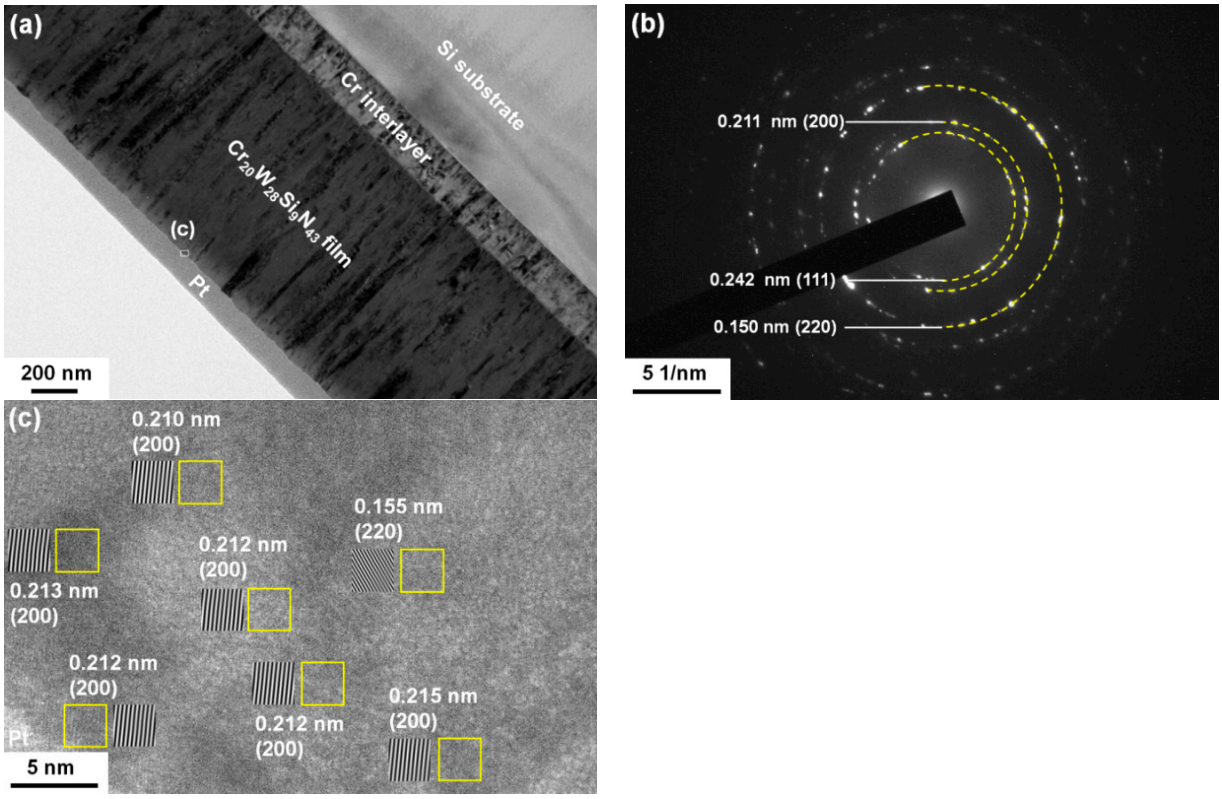


**Figure 3.** (**a**) XTEM image and (**b**) SAED pattern of the as-deposited A50T(400) sample, and (**c**) HRTEM image of the area indicated in (**a**).

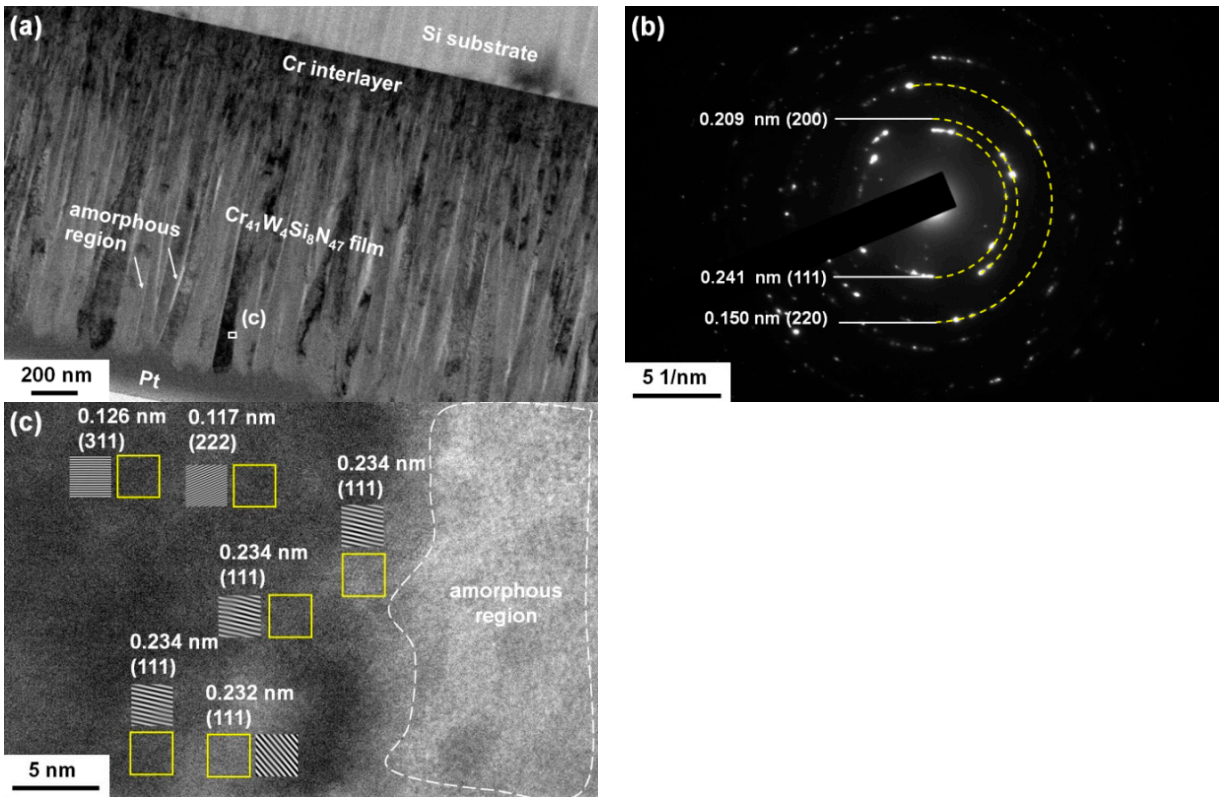


**Figure 4.** (**a**) XTEM image and (**b**) SAED pattern of the as-deposited A90B(100) sample, and (**c**) HRTEM image of the area indicated in (**a**).

### 3.2. Mechanical Properties

Table 3 shows the mechanical properties of the CrWSiN films. The Batch 50 samples with a similar chemical composition of $Cr_{20–26}W_{20–28}Si_{7–10}N_{42–47}$ exhibited distinct mechanical properties. The A50 sample possessed a hardness ($H$) of 25.0 GPa and an elastic modulus ($E$) of 323 GPa, whereas the A50B(100) sample prepared under a $V_B$ of −100 V revealed lower $H$ and $E$ values of 20.4 and 255 GPa, respectively. In contrast, the A50T(400) sample fabricated at an elevated $T_S$ of 400 °C exhibited higher $H$ and $E$ values of 42.6 and 459 GPa, respectively. Moreover, the A50BT sample prepared at a $V_B$ of −100 V and a $T_S$ of 400 °C showed $H$ and $E$ values of 40.6 and 439 GPa, respectively, which are higher than those of A50 and A50B(100) and slightly lower than those of the A50T(400) sample. Moreover, the Batch 90 films demonstrated a variation tendency in mechanical properties similar to that of the Batch 50 films, i.e., the mechanical properties revealed that A90T(400) > A90BT > A90 > A90B(100).

**Table 3.** Mechanical properties, residual stresses, and crystallite sizes of CrWSiN films.

| Sample | $H$ [1] (GPa) | $E$ [2] (GPa) | $H/E$ | $H^3/E^2$ [3] (GPa) | $We$ [3] (%) | Stress (GPa) | $D$ [4] (nm) |
|---|---|---|---|---|---|---|---|
| A50 | 25.0 ± 0.6 | 323 ± 8 | 0.078 | 0.153 | 61 | −0.84 ± 0.22 | 44 |
| A50B(50) | 20.8 ± 2.6 | 267 ± 17 | 0.078 | 0.126 | 54 | −0.08 ± 0.08 | 51 |
| A50B(100) | 20.4 ± 1.0 | 255 ± 6 | 0.080 | 0.131 | 54 | −0.05 ± 0.01 | 51 |
| A50B(150) | 25.3 ± 0.9 | 278 ± 8 | 0.091 | 0.210 | 59 | −1.19 ± 0.18 | 43 |
| A50T(300) | 26.5 ± 1.4 | 291 ± 9 | 0.091 | 0.220 | 59 | −0.21 ± 0.18 | 47 |
| A50T(400) | 42.6 ± 0.9 | 459 ± 11 | 0.093 | 0.367 | 72 | −0.69 ± 0.05 | 37 |
| A50BT | 40.6 ± 2.2 | 439 ± 21 | 0.092 | 0.347 | 71 | −0.42 ± 0.16 | 25 |
| A90 | 8.6 ± 1.1 | 208 ± 17 | 0.041 | 0.015 | 35 | 0.23 ± 0.05 | 62 |
| A90B(100) | 6.6 ± 0.7 | 179 ± 7 | 0.037 | 0.009 | 31 | 0.26 ± 0.04 | 77 |
| A90T(400) | 26.2 ± 2.3 | 369 ± 26 | 0.071 | 0.132 | 59 | 0.58 ± 0.07 | 37 |
| A90BT | 24.4 ± 1.1 | 355 ± 21 | 0.069 | 0.115 | 58 | 0.49 ± 0.17 | 40 |

[1] $H$: hardness. [2] $E$: elastic modulus. [3] $We$: elastic recovery. [4] $D$: crystallite size.

Crystalline structure, crystalline texture, residual stress, and crystallite size affected the mechanical properties of the nitride films. The Batch 50 and 90 samples exhibited chemical compositions of $Cr_{20–26}W_{20–28}Si_{7–10}N_{42–47}$ and $Cr_{37–41}W_{4–5}Si_{8–10}N_{47–49}$, respectively, and such CrWSiN films belonged to CrSiN-dominated structures [9]. CrSiN [30] and WSiN [4] films crystallized into a rock salt structure, and these films with a (200) texture were reported to be harder than the films with a (111) texture. Figure 5a displays the hardness values of CrWSiN films related to their texture coefficients of reflection (200) [$T_c$(200)]. The hardness value increased from 20.4 GPa for the A50B(100) film with a $T_c$(200) value of 0.01 to 20.8, 25.0, 25.3, 26.5, and 42.6 GPa for the A50B(50), A50, A50B(150), A50T(300), and A50T(400) films with $T_c$(200) values of 0.015, 0.04, 0.04, 0.16, and 0.29, then slightly decreased to 40.6 GPa for the A50BT film with a $T_c$(200) value of 0.56. In a previous study [16], CrSiN prepared at a $V_B$ of 0 to −75 V exhibited a hardness level of 13–14 GPa, and a higher $H$ value of 19.5 GPa was obtained when the CrSiN film was prepared at −100 V. The hardness and $T_c$(200) values of the A50B(50) films were similar to those of the A50B(100) film, although A50B(50) and A50B(100) were prepared at $V_B$ values of −50 V and −100 V, respectively. The increase in $H$ to 25.3 GPa by changing $V_B$ was observed for the A50B(150) prepared at a $V_B$ of −150 V. However, the increased hardness value as a result of applying a substrate bias was far lower than the effect caused by an elevated substrate temperature. Moreover, the hardness level increased from 6.6 GPa for the A90B(100) film with a $T_c$(200) value of 0 to 8.6, 24.4, and 26.2 GPa for the A90, A90BT, and A90T(400) films with $T_c$(200) values of 0.06, 0.09, and 0.13, respectively. In a previous study [16], CrSiN films with $T_c$(200) values higher than 1.5 exhibited hardness values of 13–22 GPa. The texture of CrWSiN films was not the primary factor that affected their mechanical properties. Figure 5b depicts the hardness values of CrWSiN films related to their residual stress values. The Batch 50 samples exhibited compressive residual stresses, whereas the Batch 90 samples exhibited tensile stresses. However, no specific relationship was obeyed between the hardness and

stress values of these CrWSiN films. For example, the A50 sample possessed an $H$ value of 25.0 GPa accompanied by a compressive stress of –0.84 GPa; in contrast, the A90T(400) sample showed a higher $H$ value of 26.2 GPa and tensile stress of 0.58 GPa, which disagrees with the conventional judgment, that is, that compressive stress increases film hardness [31]. Figure 6a depicts the relationship between the hardness and crystallite size values of the CrWSiN films. The films with smaller crystallite sizes had higher hardness values. CrWSiN films prepared at 400 °C (A50T(400), A50BT, A90T(400), and A90BT) exhibited smaller crystallite sizes compared to the films prepared without heating the substrate holder, and this phenomenon was consistent with that observed in the study of CrSiN films due to the increased nucleation rate at 400 °C [16]. In contrast, the film A50T(300) fabricated at 300 °C exhibited a larger crystallite size than those prepared at 400 °C. The main factor affecting the crystallite size could be attributed to the formation of the amorphous $SiN_x$ tissue phase in the nanocomposite nitride coatings. Benkahoul et al. [7] proposed that Si atoms segregate on the CrN grain surface and form amorphous $SiN_x$, which restricts the crystallite sizes. High-temperature processes provide higher mobility for the adatoms to move on the free surface. When amorphous $SiN_x$ was distributed homogeneously, the crystallized $CrN/W_2N$ phase exhibited a smaller nucleation size and a larger nucleation number related to the films deposited at a low substrate temperature. Figure 6b displays the relationship between elastic modulus and crystallite size, demonstrating a tendency similar to that between hardness and crystallite size. In summary, a $V_B$ of −100 V negatively affected the mechanical properties, whereas a $T_S$ of 400 °C increased the mechanical properties of the CrWSiN films. The average crystallite size dominantly affected the mechanical properties (hardness and elastic modulus) of CrWSiN films.

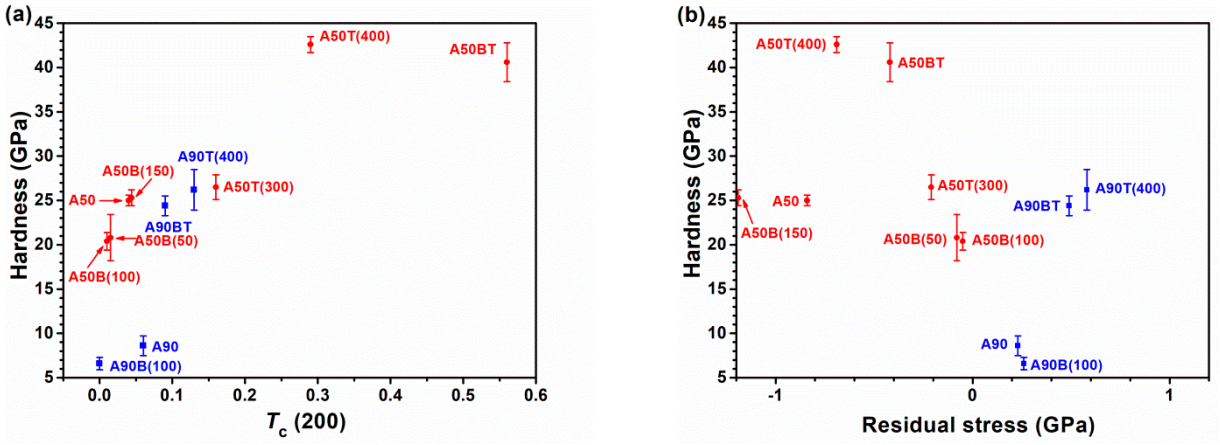


**Figure 5.** Relationships between $H$ and (**a**) $T_c$(200) and (**b**) residual stress of the CrWSiN films.

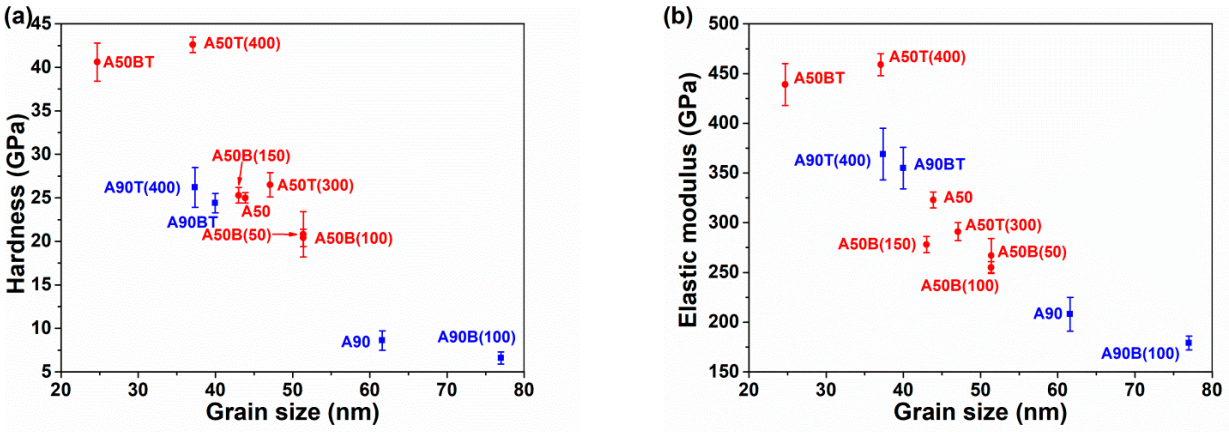


**Figure 6.** Relationships between (**a**) $H$ and (**b**) $E$ and crystallite size of the CrWSiN films.

The $H/E$ ratio [32] was used as an indicator for estimating the toughness of the films. Moreover, the $H^3/E^2$ ratio [33] was used as a gauge for evaluating the wear-resistant property of films. However, the wear resistance of the CrSiN films was not equal to that predicted by $H/E$ and $H^3/E^2$ values [16]. The usefulness of $H/E$ and $H^3/E^2$ in predicting film toughness was restricted for films with low plasticity [34]. The characteristics of interfaces, defects, and residual stresses on nanoscale films could affect their fracture toughness. Figure 7 depicts the relationship between $H$ and $E$ for CrSiN [2,16], WSiN [4,35], and CrWSiN [9] films fabricated using the same sputter apparatus. The data for Batches 50 and 90 samples are identified in this figure. The A50T(400) and A50BT samples possessed high $H/E$ ratios of 0.092–0.093 (Table 3), whereas the A50, A50B(100), A90T(400), and A90BT samples showed median $H/E$ ratios of 0.069–0.080, and the A90 and A90B(100) samples revealed low $H/E$ levels of 0.037–0.041. Table 3 shows that the Batch 50 and 90 samples can be categorized into high, median, and low ranges of $H^3/E^2$ and elastic recovery ($We$), the same as those classified by the $H/E$ ratio. Figure 8 shows the wear scars of the selected Batch 50 and 90 samples prepared on SUS420 substrates. The A90B(100) sample exhibited the lowest $H$, $E$, $H/E$, and $H^3/E^2$ values among the surveyed CrWSiN films in this study. The wear track of the A90B(100) sample revealed plastically deformed morphology, similar to that observed for the A90 sample [9]. For the films with median $H/E$, $H^3/E^2$, and $We$ values, except for the A90T(400) sample, cracks occurred on the wear scars. Table 4 lists the wear test results. The wear rate of the A90BT sample was underestimated due to crack formation, and these crack fragments still adhere to the worn part. Crack formation and propagation could be induced by the residual tensile stress of the films [36]. The A90BT sample exhibited a tensile stress of 0.49 GPa, and the A50B(100) sample possessed a near-zero stress of −0.05 GPa, which could be the reason for the formation of cracks during wear tests. However, the wear track of the A90T(400) sample was similar to those of the A50T(400) and A50BT samples, which were smooth in most portions, although the A90T(400) and A90BT samples possessed similar mechanical properties and residual tensile stresses. The deviation between the thickness values of the A90T(400) (701 nm) and A90BT (937 nm) samples should be considered and requires further investigation. The wear rates of the A90T(400), A50T(400), and A50BT samples were $1.2 \times 10^{-7}$, $8.5 \times 10^{-6}$, and $6.3 \times 10^{-6}$ mm$^3$/(N·m), respectively. In summary, the CrWSiN films with low, median, and high mechanical properties and their $H/E$ and $H^3/E^2$ ratios exhibited plastically deformed, crack-formed, and flattened worn morphologies, respectively. Figure 9 exhibits the coefficients of friction (COFs) recorded during the wear tests. Table 4 shows the average COFs at a 50–100 m wear distance. The COF of A90BT exhibited a high value of 0.63, indicating the effect of crack formation during testing. In contrast, the COFs of A90 and A90B(100) were 0.39 and 0.45, respectively, which corresponds to the occurrence of plastic deformation. The COFs of A90T(400), A50T(400), and A50BT were in the range of 0.46–0.50.

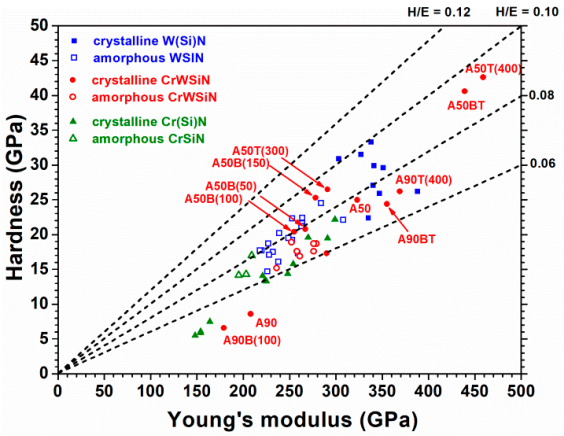


**Figure 7.** Relationship between $H$ and $E$ for (Cr,W)(Si)N films [2,4,9,16,35].

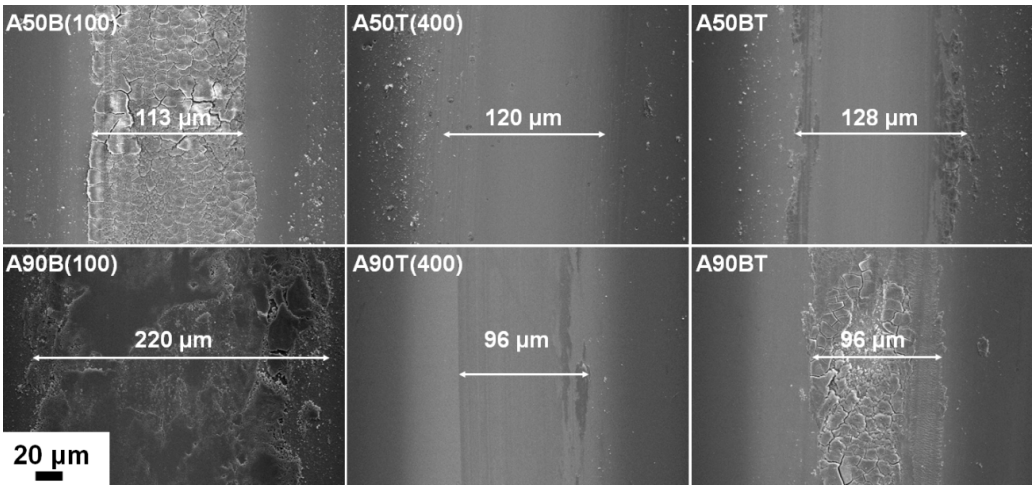


**Figure 8.** Wear scars of the CrWSiN films.

**Table 4.** Wear test results of CrWSiN films.

| Sample | $T$ [1] (nm) | Wear Depth (nm) | Wear Width (μm) | $\mu$ [2] | Wear Rate ($mm^3/(N \cdot m)$) |
|---|---|---|---|---|---|
| A50 | 705 | 1120 | 129 | 0.56 | $3.6 \times 10^{-5}$ |
| A50B(100) | 794 | 433 | 94 | 0.51 | $1.1 \times 10^{-5}$ |
| A50T(400) | 700 | 497 | 83 | 0.47 | $8.5 \times 10^{-6}$ |
| A50BT | 719 | 321 | 164 | 0.46 | $6.3 \times 10^{-6}$ |
| A90 | 880 | 1232 | 225 | 0.39 | $7.9 \times 10^{-5}$ |
| A90B(100) | 937 | 1034 | 324 | 0.45 | $2.5 \times 10^{-5}$ |
| A90T(400) | 701 | 33 | 93 | 0.50 | $1.2 \times 10^{-7}$ |
| A90BT | 707 | 61 | 108 | 0.63 | $2.6 \times 10^{-7}$ |

[1] $T$: film thickness. [2] $\mu$: coefficient of friction.

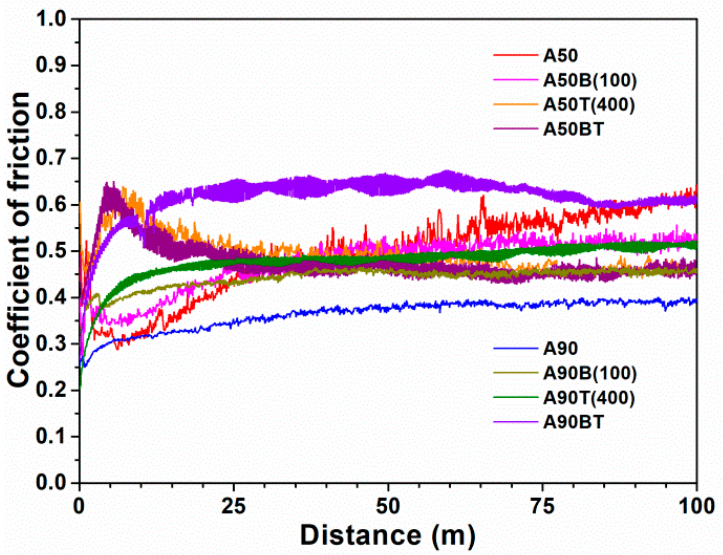


**Figure 9.** COFs of the CrWSiN films during the wear test.

### *3.3. Oxidation Behavior*

Figure 10a,b depicts the GIXRD patterns of the A50T(400), A50BT, A90T(400), and A90BT samples annealed in ambient air for 2 h at 800 and 900 °C, respectively. In a previous study [9], the GIXRD patterns of the A50 and A90 samples after 2 h of annealing at 800 °C exhibited a $Cr_2WO_6$ phase. The oxide phases of the A50T(400) and A50BT samples after

annealing at 800 °C were dominated by $Cr_2WO_6$, and transformed to mixed $Cr_2WO_6$ and $Cr_2O_3$ when annealed at 900 °C. In contrast, the A90T(400) and A90BT samples exhibited a $Cr_2O_3$ phase accompanied by the original fcc nitride phase after annealing at 800 and 900 °C, which implies that only the upper part of the A90T(400) and A90BT films were oxidized. Figure 11 depicts the surficial morphologies of the 800 °C annealed CrWSiN films. Pores were observed in the crystallite corners of the A50T(400) sample due to nitrogen-loss behavior during annealing [4]. Moreover, larger oxide grains and pores are present on the surface of the A50BT sample. In contrast, the oxide scales of the A90T(400) and A90BT samples comprised needle $Cr_2O_3$ grains, and the $Cr_2O_3$ grains on the A90BT sample were more significant than those that grew on the surface of the A90T(400) sample. Figure 12 shows cross-sectional SEM (XSEM) images of the 800 °C annealed CrWSiN films. A bi-layered oxide structure formed above the columnar A50T(400) sample, similar to that observed on the A50 sample after annealing at 800 °C for 2 h [9]. The outer oxide layer of approximately 180 nm formed above the original surface of the A50T(400) sample, whereas the inner oxide layer of 220 nm indicated the inward diffusion of O. A detailed observation on the oxide layers was performed using the XTEM image, as discussed later. In contrast, locally grown oxides were observed on the surface of the A50BT sample (Figure 11), which implies that the oxide layer thickness observed from the XESM image is uncertain. The surface oxide layers of the A90T(400) and A90BT samples were 150–180 nm, with embedded pore channels within stacked $Cr_2O_3$ grains.

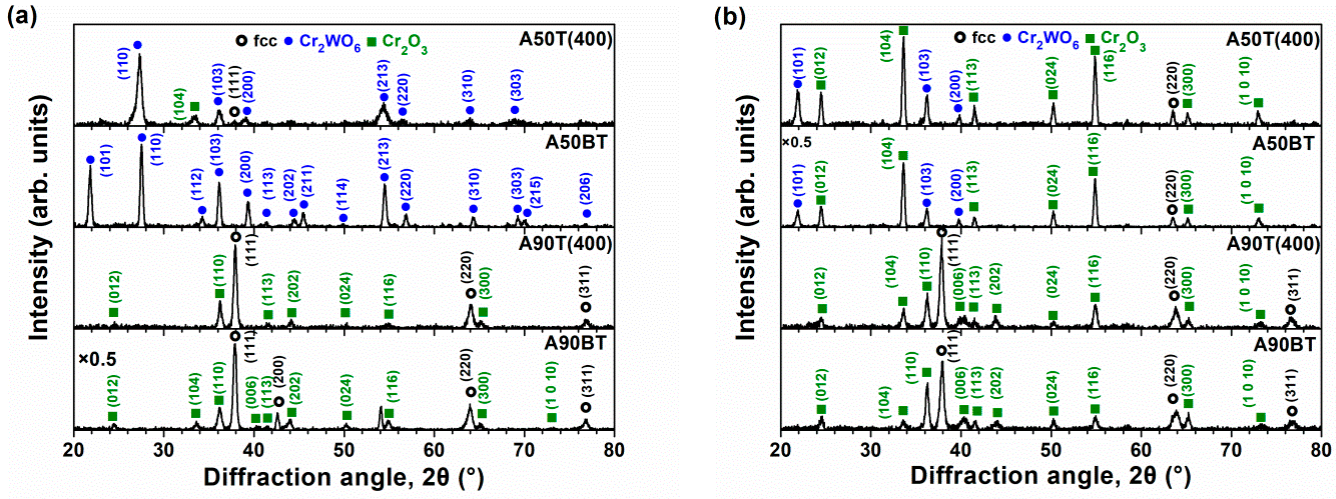


**Figure 10.** GIXRD patterns of the A50T(400), A50BT, A90T(400), and A90BT samples after 2 h of annealing at (**a**) 800 and (**b**) 900 °C.

Figure 13a displays an XTEM image of the 800 °C annealed A50T(400) sample comprising three regions, A, B, and C, with distinct morphologies. The outer oxide layer (Region A) consisted of larger $Cr_2WO_6$ grains and rod-like $Cr_2O_3$ grains (Figure 13b). The rod-like grains grew from beneath medium grains. Figure 13c,d displays HRTEM images related to $Cr_2WO_6$ and $Cr_2O_3$ grains, respectively. The lattice fringes with *d*-spacing values of 0.247–0.248 nm in the larger grains indicate $Cr_2WO_6$ (103) planes. The rod-like grains exhibited lattice fringes with *d*-spacing values of 0.266–0.267 and 0.363–0.364 nm representing the $Cr_2O_3$ (104) and (012) planes. The portion interlaid with larger and rod-like grains had *d*-spacing values of 0.247–0.248 nm, which could be either the $Cr_2WO_6$ (103) or $Cr_2O_3$ (110) planes. Region B, located beneath the original surface, comprised smaller $Cr_2WO_6$ grains (Figure 13e). Region C exhibited columnar CrN/$W_2N$ grains (Figure 13f).

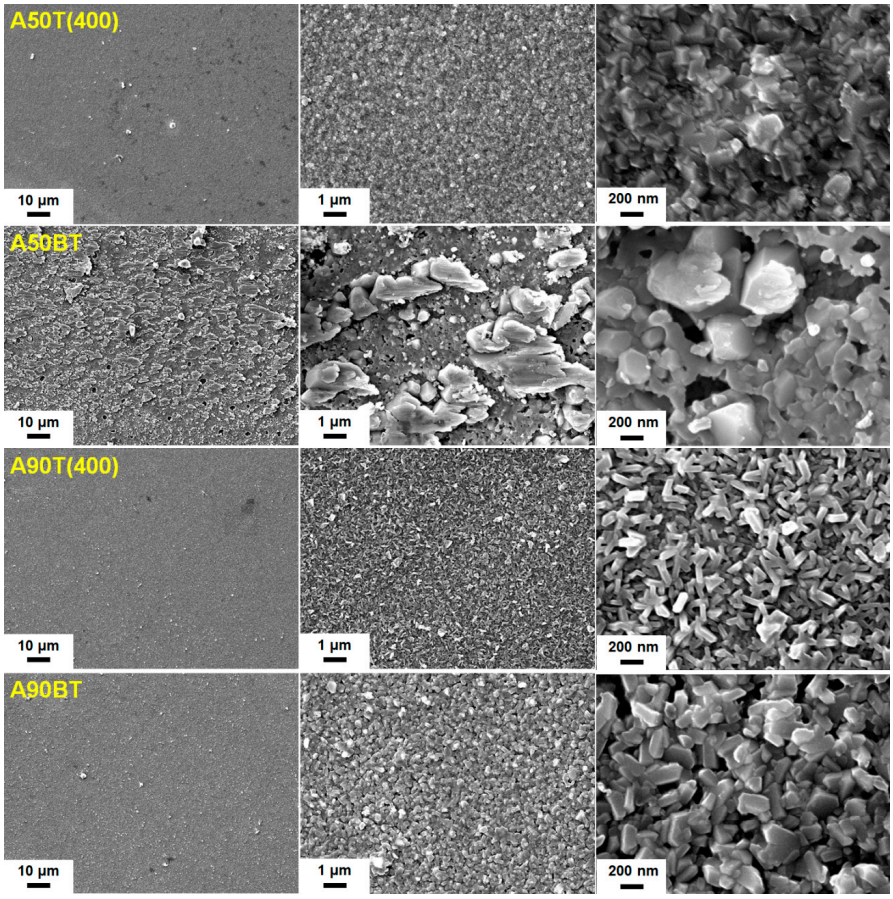


**Figure 11.** Surficial SEM morphologies of the A50T(400), A50BT, A90T(400), and A90BT samples after 2 h of annealing at 800 °C.

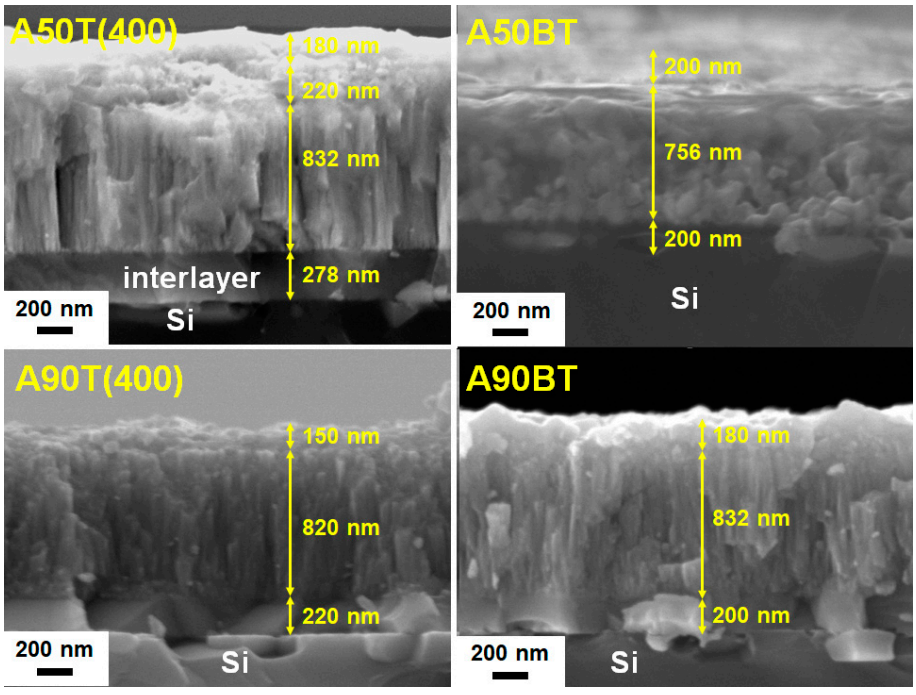


**Figure 12.** XSEM images of the 800 °C annealed A50T(400), A50BT, A90T(400), and A90BT samples.

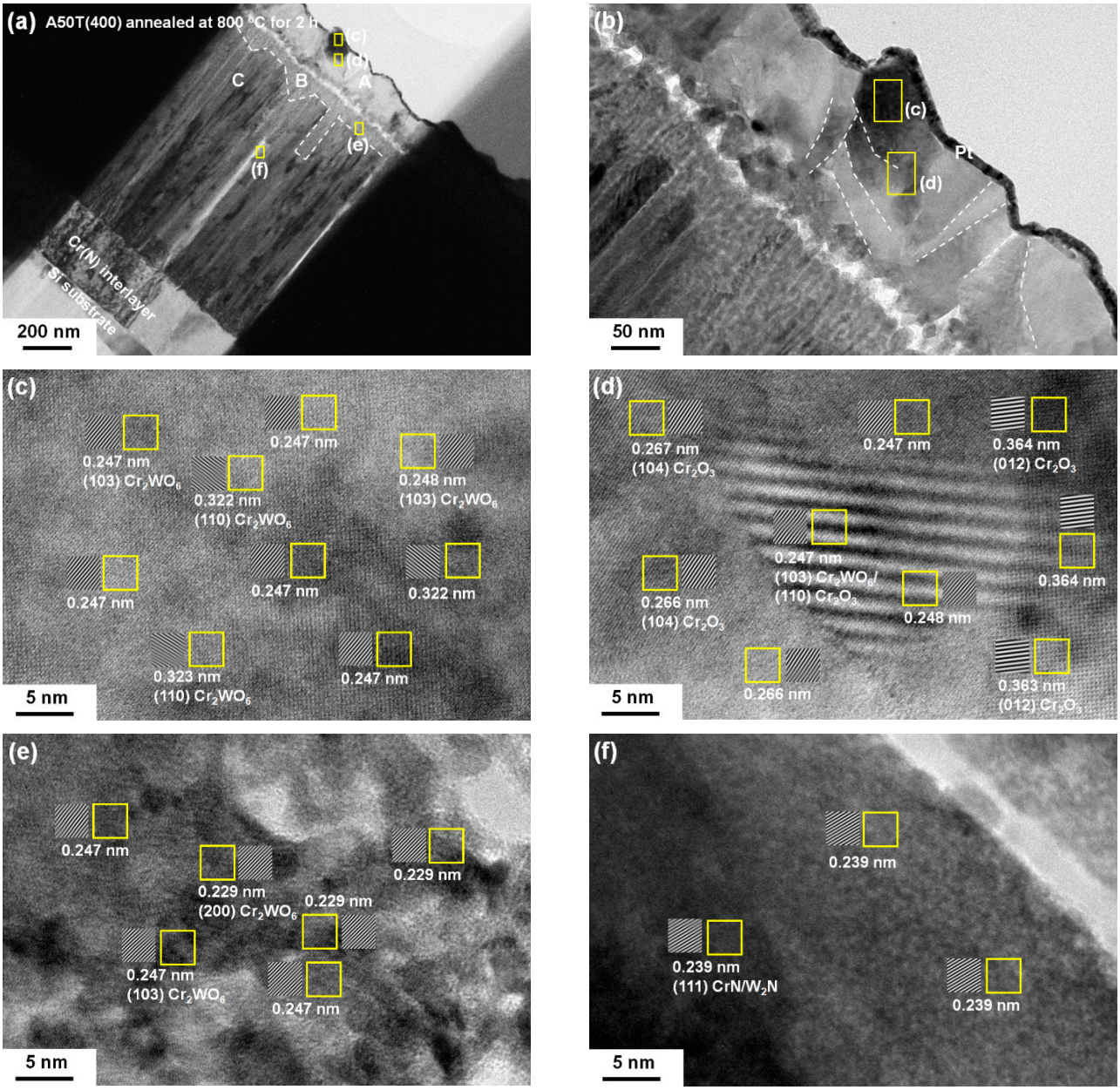


**Figure 13.** (**a**,**b**) XTEM and (**c**–**f**) HRTEM images of the A50T(400) sample after annealing at 800 °C for 2 h.

Figure 14a depicts an XTEM image of the 800 °C annealed A90T(400) sample. Three regions, I, II, and III, are distinguished. Regions I and III are also shown in the XSEM image (Figure 12), whereas Region II could not be indicated in the XSEM image. Region I shows that precipitations extrude above the original surface, whereas the columnar structure accompanied by amorphous boundaries is observed in Region III. Figure 14b,c exhibits the SAED patterns of Regions I and III, which exhibit the $Cr_2O_3$ and $CrN/W_2N$ phases, respectively. The $Cr_2O_3$ precipitations are large, so its SAED pattern represents a single crystal. Figure 14d displays an HRTEM image of Region I and related lattice fringes, indicating that these precipitations are $Cr_2O_3$. Also observed in Figure 11 is that these extruded $Cr_2O_3$ precipitations stack on top of each other, and voids appear that cause difficulty in protecting from inward oxidation. Figure 14e shows an HRTEM image of Region II that exhibits crystalline $Cr_2O_3$ domains with sizes of several nanometers. The dense Region II plays the role of advancing the oxidation resistance of CrWSiN films.

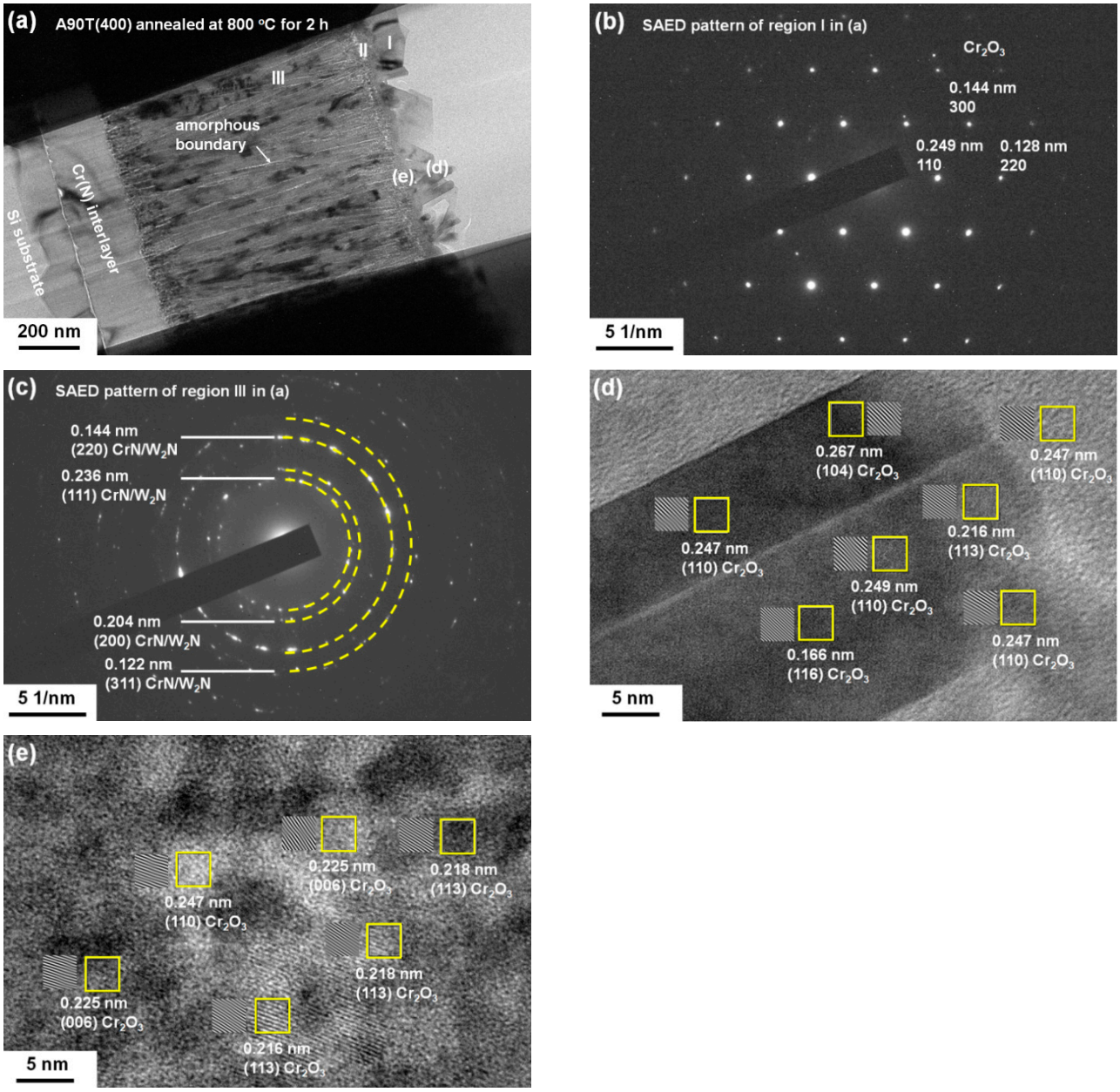


**Figure 14.** (**a**) XTEM image, (**b**,**c**) SAED patterns, and (**d**,**e**) HRTEM images of the 800 °C and 2 h annealed A90T(400) sample.

Figures 15 and 16 show the XSEM images and surficial morphologies of the 900 °C annealed CrWSiN films. Oxide grains with dimensions of several microns were observed on the surfaces of the A50T(400) and A50BT samples. Circular dark parts on the A50BT sample imply the formation and removal of buckle oxides. In contrast, the oxidation behavior of the A90T(400) and A90BT samples at 900 °C was similar to that of these samples annealed at 800 °C. A $Cr_2O_3$ layer restricted the inward diffusion of oxygen. However, the $Cr_2O_3$ grains were round (Figure 16) but not rod-like as observed for the 800 °C annealed A90T(400) sample (Figure 11). Figure 17a depicts an XTEM image of the A90T(400) sample after annealing at 900 °C for 2 h. Compared with Figure 14a, Figure 17a displays that the three regions (I, II, and III) are sustained, and the thicknesses of Regions I and II are enlarged. Figure 17b,c displays the SAED pattern and HRTEM image of Region I of the 900 °C annealed A90T(400) sample, respectively, implying that the $Cr_2O_3$ phase dominates Region I. Region II exhibited mixed oxides of $Cr_2O_3$, $Cr_2WO_6$, and $WO_3$ (Figure 17d). The SAED

pattern of Region III exhibited $Cr_2O_3$, $WO_3$, and fcc ($CrN/W_2N$) phases (Figure 17e). In summary, A90T(400) and A90BT samples exhibited superior oxidation resistance compared to the A50T(400) and A50BT samples at 900 °C.

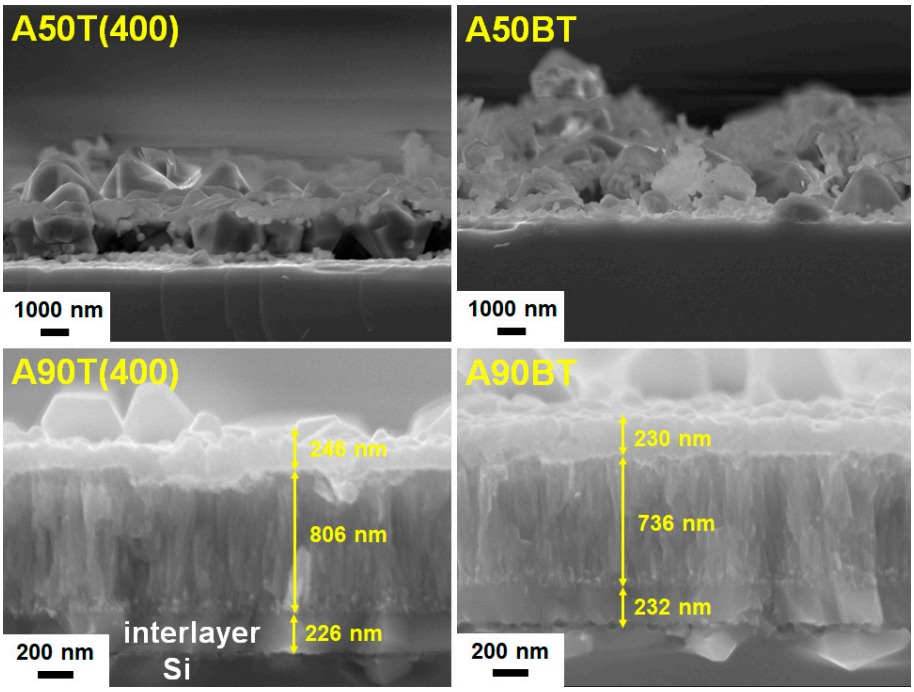


**Figure 15.** XSEM images of the 900 °C annealed A50T(400), A50BT, A90T(400), and A90BT samples.

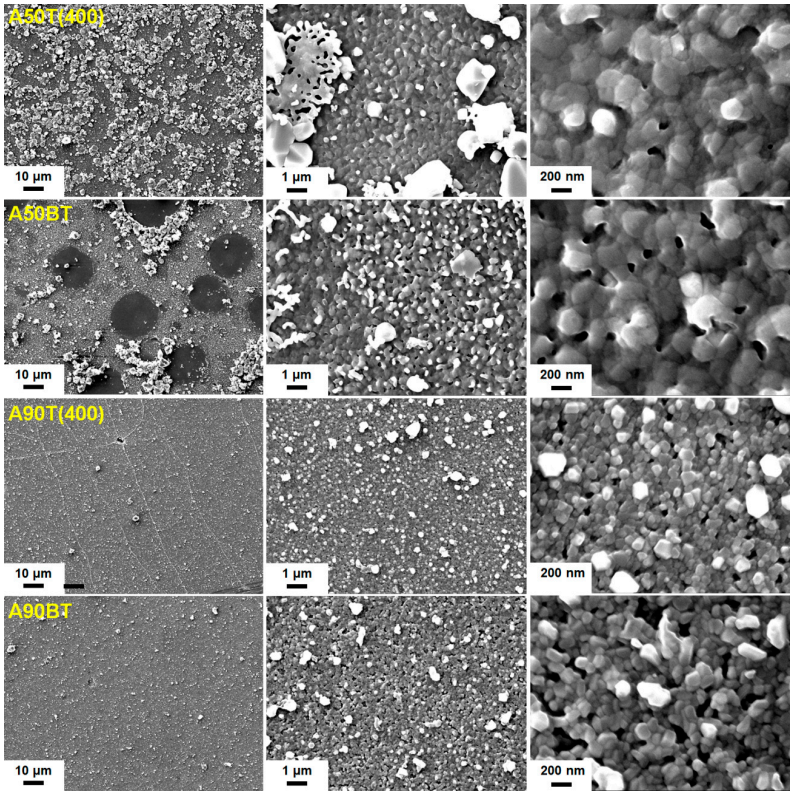


**Figure 16.** Surficial SEM morphologies of the A50T(400), A50BT, A90T(400), and A90BT samples after 2 h of annealing at 900 °C.

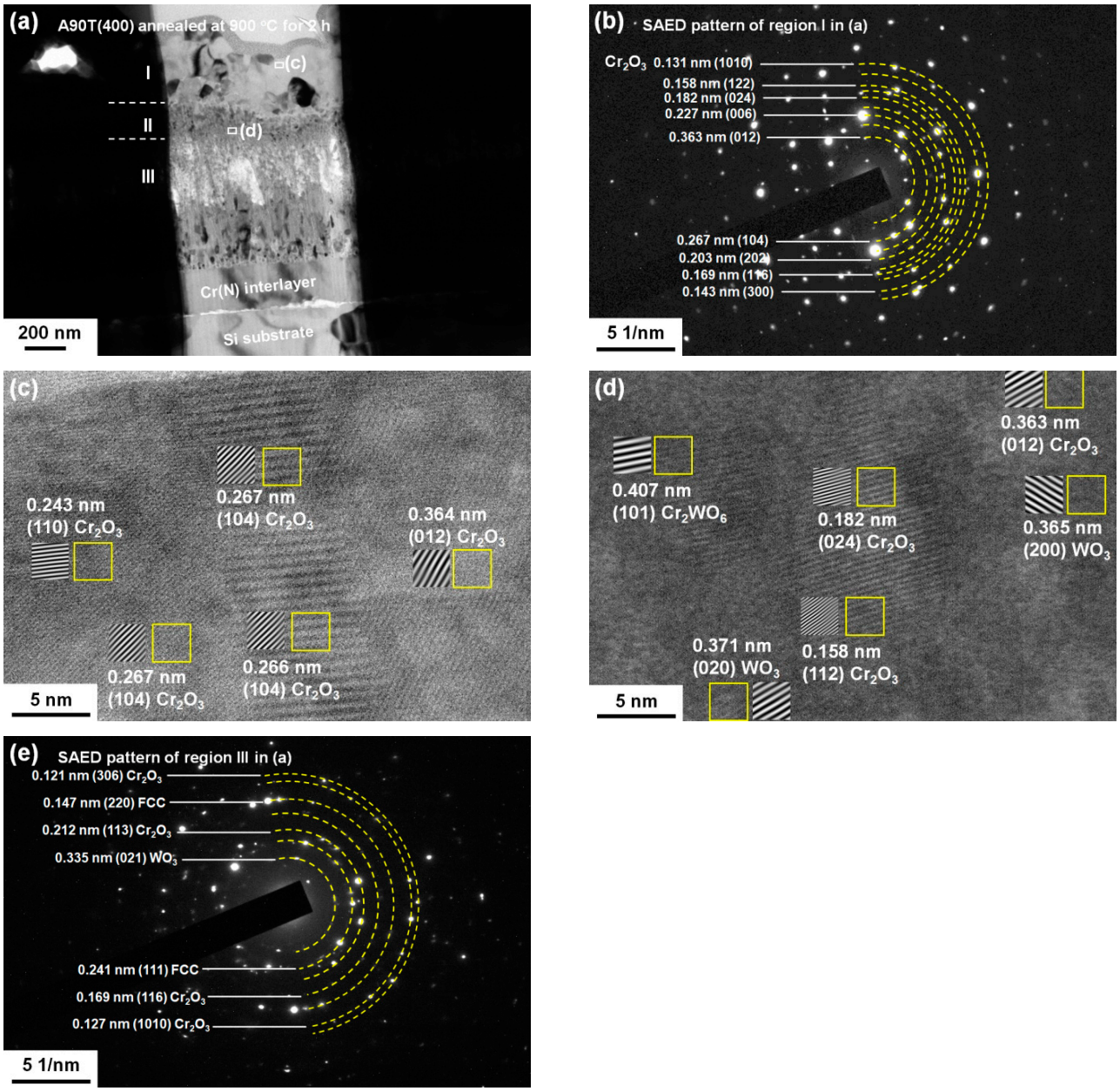


**Figure 17.** (**a**) XTEM image, (**b**,**e**) SAED patterns, and (**c**,**d**) HRTEM images of the A90T(400) sample after annealing at 900 °C for 2 h.

## 4. Conclusions

The effects of substrate bias voltage and temperature on the characteristics of CrWSiN films were studied. Two batches of CrWSiN films were fabricated, $Cr_{20–26}W_{20–28}Si_{7–10}N_{42–47}$ and $Cr_{37–41}W_{4–5}Si_{8–10}N_{47–49}$, which were near-equal Cr and W and Cr-enriched films, respectively. The effects of $V_B$ and $T_S$ on macroscopic properties, such as the films' chemical compositions and macrostructures were insignificant, as observed from their EPMA results and XRD patterns. In contrast, the mechanical properties, hardness and elastic modulus, of the CrWSiN films were dominantly affected by their average crystallite size. The effect of $T_S$ was more evident than that of $V_B$. The $Cr_{20}W_{28}Si_9N_{43}$ and $Cr_{21}W_{28}Si_{10}N_{42}$ samples with near-equal Cr and W contents prepared at a $T_S$ of 400 °C exhibited small crystallite sizes of 37 and 25 nm, high hardness values of 42.6 and 40.6 GPa, high elastic modulus values of 459 and 439 GPa, high $H/E$ ratios of 0.093 and 0.092, and high $H^3/E^2$ ratios of 0.367 and 0.347 GPa, respectively, accompanied with low wear rates of 8.5 and 6.3 $\times$ $10^{-6}$

$mm^3/(N \cdot m)$, respectively. The decrease in crystallite sizes of the nanocomposite films at a higher $T_S$ of 400 °C was attributed to the homogeneous and random segregation of the $SiN_x$ tissue phase surrounding the $CrN/W_2N$ crystallites, resulting in higher nucleation rates in film deposition. The CrWSiN films with near-equal Cr and W contents revealed oxidation resistance at 800 °C in ambient air, whereas the Cr-enriched CrWSiN films ($Cr_{37}W_4Si_{10}N_{49}$ and $Cr_{37}W_5Si_{10}N_{48}$) exhibited higher oxidation resistance up to 900 °C. The surficial $Cr_2O_3$ layer restricted the progression of oxidation.

**Author Contributions:** Conceptualization, Y.-I.C.; validation, L.-C.C., C.-H.T. and T.-Y.O.; formal analysis, C.-H.T. and T.-Y.O.; investigation, C.-H.T. and T.-Y.O.; resources, L.-C.C. and Y.-I.C.; writing—original draft preparation, Y.-I.C.; supervision, Y.-I.C.; project administration, Y.-I.C.; funding acquisition, L.-C.C. and Y.-I.C. All authors have read and agreed to the published version of the manuscript.

**Funding:** This research was funded by the National Science and Technology Council, Taiwan, grant numbers 111-2221-E-019-064 and 111-2221-E-131-028. The APC was funded by National Taiwan Ocean University.

**Institutional Review Board Statement:** Not applicable.

**Informed Consent Statement:** Not applicable.

**Data Availability Statement:** Not applicable.

**Acknowledgments:** The analysis support from the Joint Center for High Valued Instruments at NSYSU for the FIB is acknowledged. The analysis support from the Instrumentation Center at National Tsing Hua University for the EPMA is appreciated.

**Conflicts of Interest:** The authors declare no conflict of interest.

## References

1. Diyatmika, W.; Cheng, C.Y.; Lee, J.W. Fabrication of Cr-Si-N coatings using a hybrid high-power impulse and radio-frequency magnetron co-sputtering: The role of Si incorporation and duty cycle. *Surf. Coat. Technol.* **2020**, *403*, 126378. [CrossRef]
2. Chang, L.C.; Liu, Y.H.; Chen, Y.I. Mechanical properties and oxidation behavior of Cr–Si–N coatings. *Coatings* **2019**, *9*, 528. [CrossRef]
3. Ju, H.; He, S.; Yu, L.; Asempah, I.; Xu, J. The improvement of oxidation resistance, mechanical and tribological properties of $W_2N$ films by doping silicon. *Surf. Coat. Technol.* **2017**, *317*, 158–165. [CrossRef]
4. Liu, Y.H.; Chang, L.C.; Liu, B.W.; Chen, Y.I. Mechanical properties and oxidation behavior of W–Si–N Coatings. *Surf. Coat. Technol.* **2019**, *375*, 727–738. [CrossRef]
5. Chen, H.W.; Chan, Y.C.; Lee, J.W.; Duh, J.G. Oxidation behavior of Si-doped nanocomposite CrAlSiN coatings. *Surf. Coat. Technol.* **2010**, *205*, 1189–1194. [CrossRef]
6. Dong, Y.; Zhu, H.; Ge, F.; Zhao, G.; Huang, F. Microstructural effects on the high-temperature steam oxidation resistance of magnetron sputtered Cr-Al-Si-N quaternary coatings on zirconium coupons. *Surf. Coat. Technol.* **2019**, *374*, 393–401. [CrossRef]
7. Benkahoul, M.; Robin, P.; Gujrathi, S.C.; Martinu, L.; Klemberg-Sapieha, J.E. Microstructure and mechanical properties of Cr–Si–N coatings prepared by pulsed reactive dual magnetron sputtering. *Surf. Coat. Technol.* **2008**, *202*, 3975–3980. [CrossRef]
8. Lee, J.W.; Chang, Y.C. A study on the microstructures and mechanical properties of pulsed DC reactive magnetron sputtered Cr–Si–N nanocomposite coatings. *Surf. Coat. Technol.* **2007**, *202*, 831–836. [CrossRef]
9. Chang, L.C.; Sung, M.C.; Chen, Y.I.; Tseng, C.H. Mechanical properties and oxidation behavior of CrWSiN films. *Surf. Coat. Technol.* **2022**, *437*, 128368. [CrossRef]
10. de Boer, F.R.; Boom, R.; Mattens, W.C.M.; Miedema, A.R.; Niessen, A.K. *Transition Metal Alloys*; North-Holland: Amsterdam, The Netherlands, 1988.
11. Barin, I. *Thermochemical Data of Pure Substances*, 3rd ed.; VCH: New York, NY, USA, 1995.
12. Telu, S.; Patra, A.; Sankaranarayana, M.; Mitra, R.; Pabi, S.K. Microstructure and cyclic oxidation behavior of W-Cr alloys prepared by sintering of mechanically alloyed nanocrystalline powders. *Int. J. Refract. Met. Hard Mater.* **2013**, *36*, 191–203. [CrossRef]
13. Shin, S.H.; Kim, M.W.; Kang, M.C.; Kim, K.H.; Kwon, D.H.; Kim, J.S. Cutting performance of CrN and Cr-Si–N coated end-mill deposited by hybrid coating system for ultra-high speed micro machining. *Surf. Coat. Technol.* **2008**, *202*, 5613–5616. [CrossRef]
14. Kim, C.; Kang, M.C.; Kim, J.S.; Kim, K.H.; Shin, B.S.; Je, T.J. Mechanical properties and cutting performance of nanocomposite Cr–Si–N coated tool for green machining. *Curr. Appl. Phys.* **2009**, *9*, S145–S148. [CrossRef]
15. Xiang, Y.; Huang, L.; Zou, C. Effects of bias voltages on the structural, mechanical and oxidation resistance properties of Cr–Si–N nanocomposite coatings. *Coatings* **2020**, *10*, 796. [CrossRef]
16. Chang, L.C.; Sung, M.C.; Chen, Y.I. Effects of bias voltage and substrate temperature on the mechanical properties and oxidation behavior of CrSiN films. *Vacuum* **2021**, *194*, 110580. [CrossRef]

17. Tan, S.; Zhang, X.; Wu, X.; Fang, F.; Jiang, J. Effect of substrate bias and temperature on magnetron sputtered CrSiN films. *Appl. Surf. Sci.* **2011**, *257*, 1850–1853. [CrossRef]
18. Subramanian, B.; Ananthakumar, R.; Vidhya, V.S.; Jayachandran, M. Influence of substrate temperature on the materials properties of reactive DC magnetron sputtered Ti/TiN multilayered thin films. *Mater. Sci. Eng. B* **2011**, *176*, 1–7. [CrossRef]
19. Le, V.V.; Nguyen, T.T.; Kim, S.K. The influence of nitrogen pressure and substrate temperature on the structure and mechanical properties of CrAlBN thin films. *Thin Solid Films* **2013**, *548*, 377–384. [CrossRef]
20. Ran, Y.; Lu, H.; Zhao, S.; Jia, L.; Li, Y.; Jiang, Z.; Wang, Z. Effects of substrate bias and temperature on the structure and dielectric properties of $Ti_xZr_{1-x}N_y$ ternary nitride thin films. *Surf. Coat. Technol.* **2019**, *359*, 258–264. [CrossRef]
21. Chang, L.C.; Tzeng, C.H.; Chen, Y.I. Effects of W content on structural and mechanical properties of TaWN films. *Coatings* **2022**, *12*, 700. [CrossRef]
22. Cullity, B.D.; Stock, S.R. *Elements of X-ray Diffraction*, 3rd ed.; Prentice-Hall: Hoboken, NJ, USA, 2001; pp. 169–170.
23. Oliver, W.C.; Pharr, G.M. An improved technique for determining hardness and elastic modulus using load and displacement sensing indentation experiments. *J. Mater. Res.* **1992**, *7*, 1564–1583. [CrossRef]
24. Simmons, G.; Wang, H. *Single Crystal Young's Constants and Calculated Aggregate Properties: A Handbook*; MIT Press: Cambridge, MA, USA, 1971.
25. Olaya, J.J.; Wei, G.; Rodil, S.E.; Muhl, S.; Bhushan, B. Influence of the ion–atom flux ratio on the mechanical properties of chromium nitride thin films. *Vacuum* **2007**, *81*, 610–618. [CrossRef]
26. Polcar, T.; Parreira, N.M.G.; Cavaleiro, A. Structural and tribological characterization of tungsten nitride coatings at elevated temperature. *Wear* **2008**, *265*, 319–326. [CrossRef]
27. Dai, C.L.; Chang, Y.M. A resonant method for determining mechanical properties of $Si_3N_4$ and $SiO_2$ thin films. *Mater. Lett.* **2007**, *61*, 3089–3092. [CrossRef]
28. Janssen, G.C.A.M.; Abdalla, M.M.; van Keulen, F.; Pujada, B.R.; van Venrooy, B. Celebrating the 100th anniversary of the Stoney equation for film stress: Developments from polycrystalline steel strips to single crystal silicon wafers. *Thin Solid Films* **2009**, *517*, 1858–1867. [CrossRef]
29. Wang, Q.M.; Kim, K.H. Microstructural control of Cr–Si–N films by a hybrid arc ion plating and magnetron sputtering process. *Acta Mater.* **2009**, *57*, 4974–4987. [CrossRef]
30. Martinez, E.; Sanjinés, R.; Banakh, O.; Lévy, F. Electrical, optical and mechanical properties of sputtered CrNy and $Cr_{1-x}Si_xN_{1.02}$ thin films. *Thin Solid Films* **2004**, *447–448*, 332–336. [CrossRef]
31. Bielawski, M. Residual stress control in TiN/Si coatings deposited by unbalanced magnetron sputtering. *Surf. Coat. Technol.* **2006**, *200*, 3987–3995. [CrossRef]
32. Pogrebnjak, A.D.; Beresnev, V.M.; Bondar, O.V.; Postolnyi, B.O.; Zaleski, K.; Coy, E.; Jurga, S.; Lisovenko, M.O.; Konarski, P.; Rebouta, L.; et al. Superhard CrN/MoN coatings with multilayer architecture. *Mater. Des.* **2018**, *153*, 47–59. [CrossRef]
33. Tsui, T.Y.; Pharr, G.M.; Oliver, W.C.; Bhatia, C.S.; White, R.L.; Anders, S.; Anders, A.; Brown, I.G. Nanoindentation and nanoscratching of hard carbon coatings for magnetic disks. *Mater. Res. Soc. Symp. Proc.* **1995**, *383*, 447–452. [CrossRef]
34. Chen, X.; Du, Y.; Chung, Y.W. Commentary on using $H/E$ and $H^3/E^2$ as proxies for fracture toughness of hard coatings. *Thin Solid Films* **2019**, *688*, 137265. [CrossRef]
35. Chang, L.C.; Sung, M.C.; Chu, L.H.; Chen, Y.I. Effects of the nitrogen flow ratio and substrate bias on the mechanical properties of W–N and W–Si–N films. *Coatings* **2020**, *10*, 1252. [CrossRef]
36. Vierneusel, B.; Benker, L.; Tremmel, S.; Göken, M.; Merle, B. Isolating the effect of residual stresses on coating wear by a mechanical stress relaxation technique. *Thin Solid Films* **2017**, *638*, 159–166. [CrossRef]


**Disclaimer/Publisher's Note:** The statements, opinions and data contained in all publications are solely those of the individual author(s) and contributor(s) and not of MDPI and/or the editor(s). MDPI and/or the editor(s) disclaim responsibility for any injury to people or property resulting from any ideas, methods, instructions or products referred to in the content.